Nano Research

Open Access

Research Article

Photothermal probiotics delivery of photodynamic agents for enhanced immunogenic cell death within hypoxia center of solid tumors

Wen Luo[1], Shiyu Du[1], Yateng Jiang[1], Bangshun He[2] ✉, Jun Tang[3] ✉, Jingjing Yang[4] ✉, and Yujun Song[1] ✉

[1] *Jiangsu Key Laboratory of Artificial Functional Materials, State Key Laboratory of Analytical Chemistry for Life Science, National Laboratory of Solid State Microstructures, College of Engineering and Applied Sciences, Nanjing University, Nanjing 210023, China*
[2] *Department of Laboratory Medicine, Nanjing First Hospital, Nanjing Medical University, Nanjing 210006, China*
[3] *Department of Anesthesiology, Jinling Hospital, Medical School of Nanjing University, Nanjing 210000, China*
[4] *Department of Biochemistry and Molecular Biology, School of Medicine & Holistic Integrative Medicine, Jiangsu Collaborative Innovation Center of Chinese Medicinal Resources Industrialization, Nanjing University of Chinese Medicine, Nanjing 210023, China*

Cite this article: *Nano Research*, **2025**, *18*, 94907081. https://doi.org/10.26599/NR.2025.94907081

ABSTRACT: Resulting from harsh hypoxic environmental conditions, central cells in the core of solid tumors are usually more aggressive and malignant with a less stable genome. Therefore, therapeutic agents with improved penetration for the activation of immunity in tumor centers exhibit promising potential in immunotherapies. Here, polydopamine-coated *Escherichia coli Nissle* 1917 (EcN) bearing chlorin e6 (Ce6)-loaded and polyethyleneimine (PEI)-coated hollow manganese dioxide (shorted as EP-ChP) are applied for enhanced immunotherapy in deep tumors. After accumulation in tumor center through hypoxia targeting, manganese dioxide is degradated under the tumor microenvironment with released Ce6 and thus generates reactive oxygen species (ROS) upon 660 nm laser irradiation, which can further lower thermal-resistance of cancer cells via HSP90α downregulation. Owing to that, heating induced by polydopamine upon 808 nm laser irradiation can achieve effective tumor ablation. Phototherapy upon dual laser induces enhanced immunogenic cell death, while bacterial infections in tumor tissues also trigger innate immunity. This bacteria-based approach provides enhanced antitumor immune responses in deep tumors with great potential in the reshaping of immunosuppression tumor microenvironment.

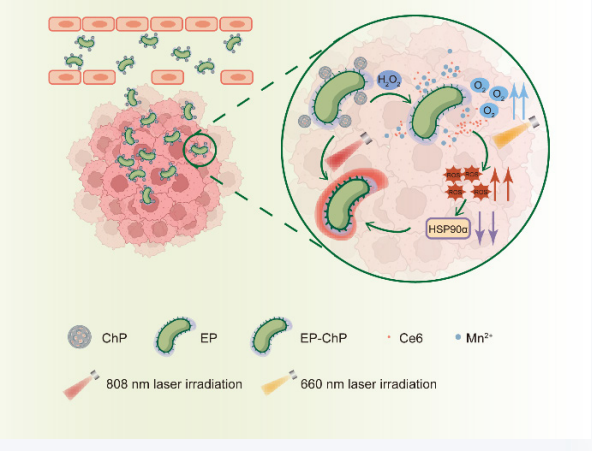

KEYWORDS: bacteria, phototherapies, immunotherapy, hypoxia targeting, tumor penetration

1 Introduction

The past decades have witnessed astounding successes in immunotherapy [1, 2], however, a majority of patients with tumors resistant to these therapies have gained minimal clinical benefit [3, 4]. Promoting antitumor immunity in such patients remains a challenge and requires an advanced understanding of the complexity of the tumor immune microenvironment (TIME), which is a deciding factor of the response to immunotherapies [5, 6]. The composition and quality of immune infiltrates into the solid tumors play important roles in tumor progression and metastasis, where immunosuppressive TIME usually acts as the barrier to immune infiltrates and results in insufficient cytotoxic lymphocytes (CTLs) in the core of tumors [7, 8]. Accordingly, regulating CTLs infiltration into solid tumors could help to remove the obstacle to efficient antitumor immunity and convert cold tumors to hot tumors [9–11]. Moreover, phenotypes of more aggressive and metastasizing subclones are reported to preferentially originate from the core of solid tumors, with a less stable genome resulting from harsh hypoxic environmental conditions with approximately less than 0.7% O_2 [12, 13]. Thus, eliciting antitumor immune

Received: July 24, 2024; **Revised:** September 12, 2024
Accepted: October 17, 2024

✉Address correspondence to Bangshun He, hebangshun@163.com; Jun Tang, nztangjun@163.com; Jingjing Yang, jingjingyang@njucm.edu.cn; Yujun Song, ysong@nju.edu.cn

responses within solid tumors with efficient penetration into deep tumors is a promising way to improve the efficacy of immunotherapy.

On the other hand, with the rocketing understanding of the microbiome/cancer partnership [14], bacteria-based cancer therapy has received increasing attention in recent decades. Both facultatively and strictly anaerobic bacteria can target tumor by virtue of their preference to colonize hypoxia and necrotic tumor cores [15, 16], which makes them ideal candidates for more efficient drug delivery with less off-targeted effect [17–19]. These hypoxia-driven vectors provide a potent potential for improved accumulation and penetration of immune adjuvant in the center of solid tumors, resulting in boosting immunotherapy with deeper spatial distributions in solid tumors [20]. Apart from drug carriers, bacteria can work as immune agents as well, where tumor microenvironment (TME) becomes potentially more immunogenic through the activation of innate immune responses via bacterial infection [21, 22]. Compared with the non-living vectors in use to date, such as liposomes [23, 24] or inorganic nanoparticles [25, 26] which mainly rely on enhanced permeability and retention (EPR) effect and systemic circulation to target tumor tissues passively [27, 28], the remarkable active targeting ability of bacteria shows great potential in penetrating solid tumors and fully eliciting antitumoral immunogenicity.

Phototherapy, including photothermal therapy (PTT) and photodynamic therapy (PDT), induced immunotherapy has emerged as a promising approach to reprogramming TIME through its ability to induce the immunogenic cell death (ICD) [29, 30]. However, immune responses caused by PTT or PDT alone are usually inadequate and short-lived. The combined therapies of PTT and PDT were proposed instead, where synergistic immunologic responses were achieved for effective anticancer treatment, especially against cancer metastasis [31, 32]. Furthermore, two different mechanisms share some mutual promotion. Reactive oxygen species (ROS) generated from PDT can attack heat shock proteins (HSPs) to promote the PTT effect [33, 34], and it has been reported that PTT could overcome hypoxia-related resistances via increased intratumoral blood flow [35]. Therefore, applying bacteria as an agent with proper self-propelling force to penetrate solid tumors for targeted co-delivery of both PDT and PTT agents could reshape immunosuppression TME with enhanced antitumor immune responses and anti-cancer efficacy.

From what has been illustrated above, we aim to harness the specific tumor-targeting ability of facultatively anaerobic bacteria *Escherichia coli Nissle* 1917 (EcN) to co-deliver PDT and PTT agents to the hypoxia core within solid tumors (Scheme 1). The synergistic nano-phototherpy platform is designed by loading photosensitizer chlorin e6 (Ce6) in polyethyleneimine (PEI)-coated

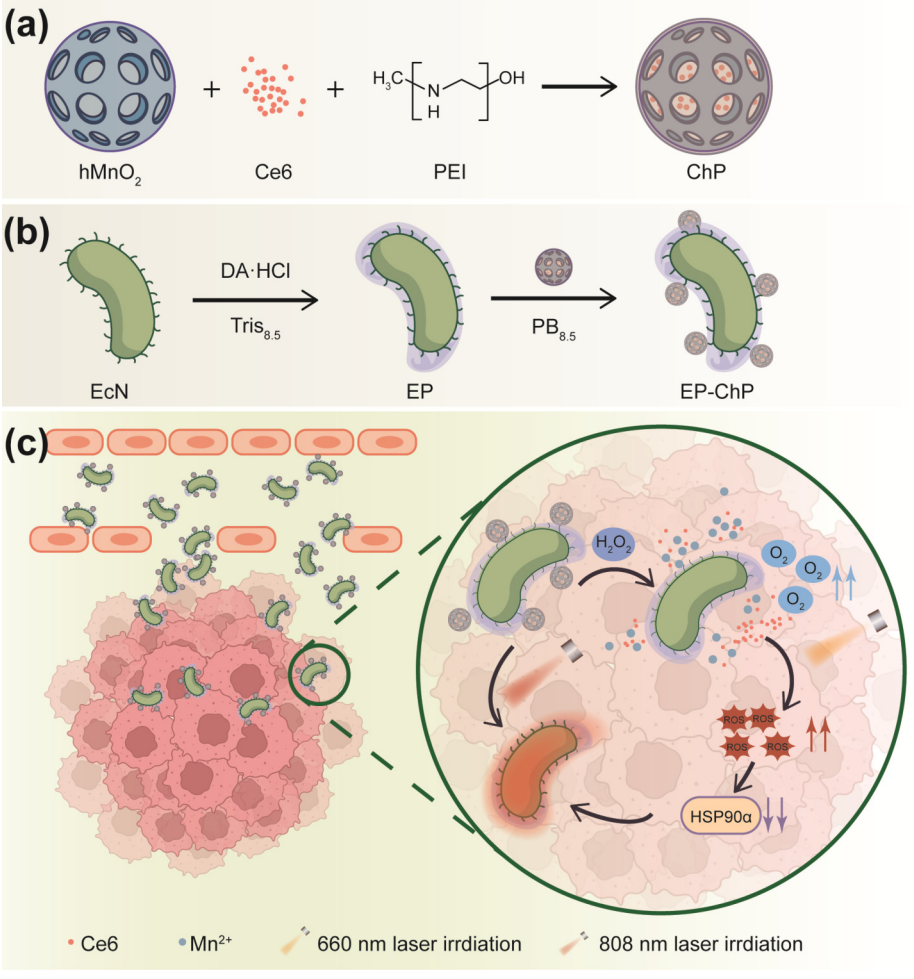

Scheme 1 Schematic illustration showing the design of the EcN-assisted PDT/PTT co-delivery and synergistic phototherapy-induced immunotherapy in the deep tumor. (a) The process for synthesis of ChP. (b) The process for synthesis of EP-ChP. (c) Schematic illustration of phototherapy-induced immunotherapy via photothermal probiotics within hypoxia center of solid tumors.

hollow manganese dioxide (shorted as $hMnO_2$), a TME-specific responsive carrier [36], which is covalently binding to polydopamine (pDA)-coated EcN (shorted as EP) afterward. Ce6 and pDA work as PDT and PTT agents respectively, and the resulting coordination immune mechanism shows enhanced local ICD *in vivo*, which is carefully examined via the elimination of primary tumors. Moreover, the immunogenicity of EcN is also an assistant to anti-tumor immune response as well as the reprogramming of immunosuppression TME.

2 Experimental

2.1 Materials

All chemical reagents were of analytical grade and used directly without further purification unless otherwise noted. Potassium permanganate ($KMnO_4$), sodium hydroxide (NaOH), ammonium hydroxide, and hydrogen peroxide (H_2O_2) were purchased from Sinopharm Chemical Reagent CO., Ltd. (Shanghai, China). Ce6 and 2',7'-dichlorodihydrofluorescein diacetate (DCFH-DA) were purchased from Sigma-Aldrich. Dopamine hydrochloride (DA), tris(hydroxymethyl)methyl aminomethane (Tris), treaethyl orthosilicate (TEOS), resorcinol, PEI, N,N-dimethylformamide (DMF), and 1,3-diphenylisobenzofuran (DPBF) were purchased from Aladdin Chemical Co. Ltd (Shanghai, China). LB broth powder, LB broth agar powder, agarose, anti-GAPDH rabbit polyclonal antibody, horseradish peroxidase (HRP)-conjugated Goat Anti-Rabbit IgG and HRP-conjugated Rabbit Anti-Mouse IgG were purchased from Sangon Biotech Co. Ltd (Shanghai, China). Normal fetal bovine serum (FBS) was purchased from ExCell Bio (Shanghai, China). HOECHST, Cell Counting Kit-8 (CCK-8) assay kit, and live/dead staining kit were purchased from Beyotime Chemical Reagent Co. Ltd (Jiangsu, China). Anti-*E. coli* lipopolysaccharide (LPS) antibody (ab35654) and anti-HSP90α antibody (ab79849) were purchased from Abcam plc (Cambridge, UK).

2.2 Preparation and characterization of ChP

$hMnO_2$ was dispersed at a concentration of 500 μg·mL^{-1}, and was stirred with various concentrations of Ce6 (125, 250, 500 and 1000 μg·mL^{-1}) in dark for 24 h for Ce6 loading. After that, Ce6@$hMnO_2$ (Ch) was collected by centrifugation (13,000 rpm, 5 min) and dispersed in H_2O. Drug loading efficiency/content was measured via free Ce6 which was removed by centrifugation at 12,000 rpm for 10 min and washed 3 times with DMF. As for the coating of PEI, PEI solution (50 μg·mL^{-1}) was added into Ch solution and stirred for 30 min to obtain the positively charged nanoparticles after washed with H_2O. Morphologies of $hMnO_2$, Ch, and ChP were characterized using transmission electron microscopy (TEM) and their ζ potentials were measured on an Anton Paar Litesizer 500.

2.3 Preparation and characterization of EP

To prepare EP, we suspended 3000 μg of dopamine hydrochloride in 3 mL of 10 mM Tris-HCl buffer (pH = 8.5) solution and then added 300 μL of the bacterial suspension. After gentle stirring at room temperature for 30 min, EP was easily obtained by centrifugation at 5000 rpm for 5 min, and then suspended in PBS. Bare EcN was used as a blank reference. Morphologies of bare EcN and EP were characterized using TEM. ζ potentials of bare EcN and EP prepared at 1000 μg·mL^{-1} dopamine were measured on an Anton Paar Litesizer 500.

2.4 Preparation and characterization of EP-ChP

To prepare EP-ChP, various amounts of ChP were added into EP suspensions. After gentle stirring at room temperature for 4 h, EP-ChP was easily obtained by centrifugation at 5000 rpm for 5 min, and then suspended in phosphate buffer saline (PBS). Morphologies of EP-ChP were characterized using TEM and ζ potentials of EP-ChP were measured on an Anton Paar Litesizer 500.

2.5 Degradation and drug release studies

$hMnO_2$ and ChP with or without H_2O_2 added were incubated 30 min under room temperature, where the remaining MnO_2 was measured every 10 min by ultraviolet–visible (UV–vis) spectra. As for drug release, ChP was incubated with different concentrations of H_2O_2 solutions (0, 1, 10, 100, and 200 mM) for 20 min under room temperature, where the fluorescence spectra of each solution were recorded on a Molecular Devices SpectraMax i3x microplate reader.

2.6 Detection of ROS *in vitro*

Free Ce6 and ChP with or without H_2O_2 added were incubated with DPBF, and then irradiated under 660-nm light for 10 min in dark at a density of 32.2 mW·cm^{-2}. And H_2O was applied as a negative control. The amounts of ROS generation at different time points were measured by UV–vis spectra.

2.7 Confocal fluorescence imaging

CT26 cells were seeded on 10 mm^2 glass coverslips placed in six-well plates and incubated with EP-ChP for various time periods (2, 4, and 8 h) in the absence of any antibiotics in the dark. After washing with PBS for three times, cells were labeled with HOECHST and imaged by a confocal laser scanning microscopy (CLSM).

2.8 ROS generation in CT26 cells

Singlet oxygen generation after PDT was determined by the DCFH-DA assay. Briefly, CT26 cells were seeded on 10 mm^2 glass coverslips placed in six-well plates and incubated with ChP, EP, or EP-ChP before they were irradiated by a 660 nm laser at a light dose of 32.2 mW·cm^{-2} for 10 min. Cells were stained by DCFH-DA assay kit and HOECHST before they were examined by CLSM.

2.9 Cytotoxicity and phototherapeutic toxicity *in vitro*

Cell viability was quantitatively evaluated by both CCK-8 assay and live/dead staining. CT26 cells were incubated for 24 h in 96-well plates at 37 °C under 5% CO_2, and then were exposed for 4 h to ChP, EP, or EP-ChP in the absence of any antibiotics. CCK-8 solution (10 μL) was added to each well, and the culture plate was incubated another 2 h before OD_{450} values of each well were measured.

To evaluate the potential synergistic phototherapy of EP-ChP on tumor cells, CT26 cells were first seeded into 96-well plates and incubated with EP-ChP for 4 h in the absence of any antibiotics. For PDT, the cells were illuminated by a 660 nm laser for different periods of time (0, 1, 3, 5, and 10 min) at various densities (32.2, 54.1, and 64.0 mW·cm^{-2}). For PTT, the cells were illuminated by an 808 nm laser for different periods of time (0, 1, 3, 5, and 10 min) at various densities (31.8, 63.6, and 95.4 mW·cm^{-2}). For PDT/PTT combination therapy, the cells were exposed to the 660 nm laser at the power density of 32.2 mW·cm^{-2} and the 808 nm laser at

31.8 mW·cm^{-2} for 5 min sequentially. After the treatments, cell viabilities were evaluated by CCK-8 assay as described previously.

The live/dead assay was implemented similarly following with the manufacturer's protocol and analyzed with a fluorescence microscopy.

2.10 *In vivo* biodistribution of EP and EP-ChP

BALB/c mice were intravenously injected with 100 μL of PBS containing 10^5 colony-forming unit (CFU) of EP or EP-ChP when tumor volumes were close to 150 mm^3, while mice intravenously injected with 100 μL of PBS were used as a negative control. Mice were sacrificed 24 h after injection, and their hearts, livers, spleens, lungs, kidneys, and tumors were collected and analyzed. All organ tissues were homogenized and serially diluted in sterile PBS, and then plated onto solid LB agar plates. The colonies on the plates were recorded after 12 h at 37 °C.

2.11 Flow cytometry analysis

Spleens obtained from mice were ground and washed by Red Blood Cell Lysis Buffer (Sangon) and filtered through 70 μm cell filters to obtain the single-cell suspensions. The cells were counted and stained with different panels of antibodies. For T cells activation analysis, cell suspensions were stained with anti-CD3 and anti-CD8 antibodies. For DC maturation analysis, cell suspensions were stained with anti-CD11c, anti-CD80, and anti-CD86 antibodies. Finally, cells were collected and analyzed by flow cytometry. All antibodies were listed in Table S1 in the Electronic Supplementary Material (ESM).

2.12 Statistical analysis and reproducibility

All experiments presented in the main manuscript and ESM were repeated at least three times. Unless clearly stated in the manuscript text, all replicate experiments were successful and confirm the presented data. For all experiments performed in BALB/c mice, at least 5 mice were randomly selected in each group. Unless clearly stated in the manuscript text, all mice showed consistent results and confirmed the presented data. From these five mice, one was selected for immunoassays.

All statistical analyses were conducted in Origin 9.8.0. And all data were obtained in triplicate and were presented as mean ± s.d. unless otherwise mentioned. Statistical analyses were performed using the *t*-test. $^*p < 0.05$, $^{**}p < 0.01$, $^{***}p < 0.001$, and $^{****}p < 0.0001$ were considered statistically significant.

3 Results and discussion

3.1 Synthesis and characterization of EP-ChP

A probiotic bacterium EcN was chosen in this bacteria-based therapy, and pDA coating was easily prepared via dopamine self-polymerization [37, 38]. $hMnO_2$ was prepared by previously reported methods [36], and Ce6 was loaded to its hollow structure through physical adsorption (shorted as Ch). To improve its hydrophilicity and extend its blood circulation, a cationic coating of PEI to the aforementioned nanoparticles was made through electrostatic interaction (shorted as ChP), which could act as both gatekeeper for Ce6 release from the carriers and bridge to EP, yielding EP-ChP, and the strategy for synthesis is illustrated in Fig. 1(a). The procedure for the synthesis of ChP is illustrated in Fig. S1(a) in the ESM and TEM images for corresponding nanoparticles with an average size of ~ 100 nm were shown in Figs. S1(b)–S1(e) in the ESM. Cell viabilities of bacteria with different treatments were examined via CCK-8 assay since only live bacteria show active tumor targeting and penetrating abilities, and as expected, both pDA coating and ChP attachment showed negligible influence on bacterial viability of EcN (Fig. 1(b)). EP showed a little more negative surface charge (–29.6 mV) than that of bare EcN (–26.6 mV), which was consistent with previously reported result [39]. And the ζ potential of EP-ChP increased to –22.2 mV after ChP attachment (Fig. 1(c)). TEM images showed native EcN with a clear edge (Fig. 1(d)) and EP with a rough layer (Fig. 1(e)), indicating a successful pDA coating upon bacteria. The special hollow nanostructures of ChP (Fig. 1(g)) on the surface of EP indicated its successful attachment (Fig. 1(f)). The surface area and average pore diameter of $hMnO_2$ were determined to be 170.308 $m^2 \cdot g^{-1}$ and 5.565 nm respectively by Brunauer–Emmett–Teller (BET) measurement (Fig. 1(h)). The porous structure makes it ideal for drug loading, hence a PDT nanoplatform could be proposed by loading photosensitizer into it. The successful loading of Ce6 was confirmed by UV–vis spectra absorbance at 660 nm, which is regarded as a characteristic peak for Ce6 (Fig. 1(i) and Figs. S3(a) and S3(b) in the ESM). The loading capacity increased with the increase of the Ce6 feeding amount while the loading efficiency went the opposite (Fig. 1(j)). And the ζ potentials of ChP with different feeding ratio were also measured. $hMnO_2$ itself had an average ζ potential of –40 mV. In contrast, as the loading of Ce6 and the coating of PEI, both Ch and ChP showed more positive ζ potentials, which was also a proof of successful modification of ChP (Fig. 1(k)). Considering both loading capacity and loading efficiency, a final feeding weight ratio (Ce6:$hMnO_2$) of 1:1 for ChP was determined for further experiments. Since ChP was fabricated through both the reactivity of pDA to primary amines of PEI and electrostatic adsorption, the exact amount of $hMnO_2$ in each feed ratio was measured by inductively coupled plasma mass spectrometry (ICP-MS) measurement (Fig. 1(l)). The exact amount of Ce6 in each feed ratio was calculated via both loading efficiency of Ce6 to $hMnO_2$ and that of ChP to EP-ChP (Fig. 1(m)). Various feed ratios of ChP to EP were also tested individually, where only limited influence on bacterial viabilities or ζ potentials of EP-ChP was found (Figs. S2(a)–S2(d) in the ESM). Considering both binding capacity of ChP and bacterial viability, a ratio of EP to ChP at 2:2 was chosen for the preparation of EP-ChP in subsequent experiments.

3.2 TME-responsive nanoparticle decomposition and drug release behaviors

$hMnO_2$ was reported to be stable under neutral environment, but specific decomposable in TME [36, 40], which is usually featured by hypoxia, low pH values, high glutathione (GSH) levels, and matrix metalloproteinases (MMPs) levels [41, 42]. The TME-responsive degradation was first confirmed by UV–vis spectra absorbance at 350 nm, which could be regarded as a characteristic peak for $hMnO_2$ in low concentration (Figs. S3(c) and S3(d) in the ESM). Quick degradation was observed within 1 h under H_2O_2 condition, which was applied as a TME stimulator (Fig. 1(n)). And as the carriers decomposed into Mn^{2+}, the release of loaded Ce6 was expected. Similar to the result above, a quick drug release was confirmed within 20 min via the fluorescence spectrum of Ce6 and the releasing rate came in a concentration-dependent manner (Fig. 1(o) and Fig. S3(e) in the ESM). Furthermore, MnO_2 is well known as a catalyst to the decomposition of H_2O_2 and the generation of

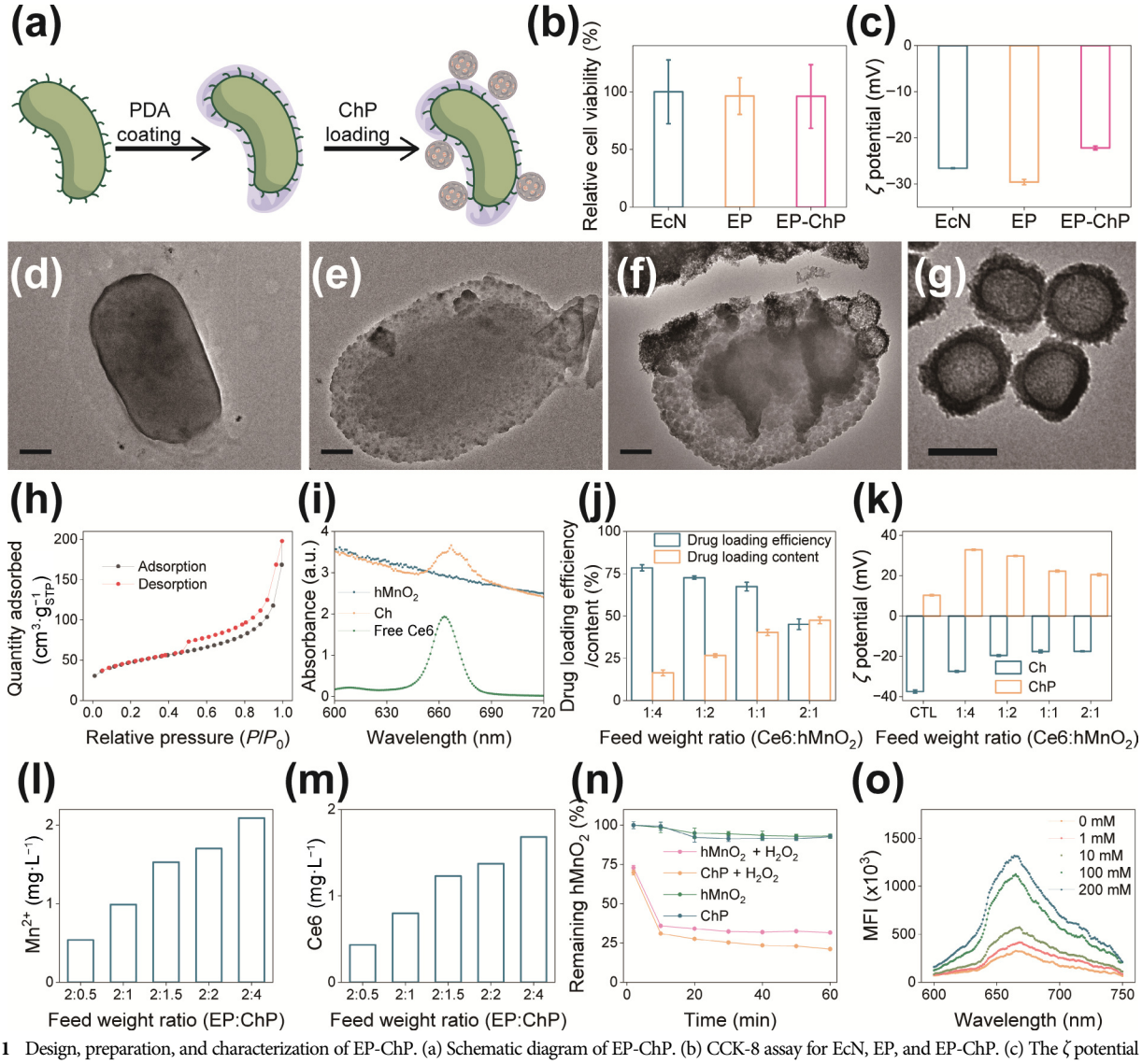

Figure 1 Design, preparation, and characterization of EP-ChP. (a) Schematic diagram of EP-ChP. (b) CCK-8 assay for EcN, EP, and EP-ChP. (c) The ζ potential of EcN, EP, and EP-ChP. TEM images of (d) EcN, (e) EP, and (f) EP-ChP. Scale bar, 200 nm. (g) TEM image of ChP. Scale bar, 100 nm. (h) N_2 adsorption–desorption isotherms of the $hMnO_2$ sample. (i) UV–vis spectra of free Ce6, $hMnO_2$, and ChP. (j) Ce6-loading efficiency/content in ChP under various weight ratios (Ce6:$hMnO_2$). (k) The ζ potential of Ch and ChP under various weight ratios (Ce6:$hMnO_2$). (l) $hMnO_2$-loading efficiency in EP-ChP under various weight ratios (EP:ChP). (m) Ce6-loading efficiency in EP-ChP under various weight ratios (EP:ChP). (n) Percentages of remaining $hMnO_2$ with or without the present of H_2O_2 solutions (100 μM). (o) Fluorescence spectra of released Ce6 from ChP under various concentrations of H_2O_2 solutions.

oxygen. This ability was also tested, where visible bubbles could be observed under H_2O_2 solutions (100 μM) (Fig. S3(f) in the ESM). The fast production of oxygen could further enhance PDT efficacy in hypoxic tumors.

3.3 *In vitro* PDT efficacy in CT26 cells

Encouraged by the as-mentioned results, the ROS-induced apoptosis under 660 nm light irradiation as the decomposition of ChP was tested (Fig. 2(a)). First, the ROS generated from free Ce6 and ChP under 660 nm light irradiation with or without the presence of H_2O_2 (100 μM) was monitored by a ROS sensor probe (DPBF) (Fig. 2(b) and Fig. S4 in the ESM). As expected, no apparent ROS production was observed in the absence of H_2O_2 regardless of light irradiation, indicating ChP could be an effective PDT agent under TME conditions. To further access the PDT effects of EP-ChP *in vitro*, murine colon carcinoma cells (CT26) were co-incubated with EP, ChP, or EP-ChP, and their cytotoxicities in the dark were tested first (Fig. 2(e) and Fig. S5 in the ESM). The CCK-8 assay indicated that EP-ChP exhibited limited toxicity to CT26 cells at a concentration of 10^8 CFU·mL^{-1} or lower. Based on that, the biodistribution of EP-ChP in cells was examined. After co-incubation with EP-ChP with the aforementioned concentration for various periods, fluorescence signals of Ce6 could be observed in cytoplasm in a time-dependent manner (Fig. 2(c) and Fig. S6(a) in the ESM), indicating an intracellular drug release from EP-ChP as the decomposition of TME-responsive carriers. The ROS generation in CT26 cells was evaluated via the DCFH-DA assay, and the fluorescence of DCF could only be observed within cells treated with ChP or EP-ChP under 660 nm light irradiation (Fig. 2(d) and Fig. S6(b) in the ESM). Moreover, the cell viability decreases with the prolongation of irradiation time and the increase of 660 nm laser working power, which both confirm the PDT therapeutic effect in cancer cells (Fig. 2(f)).

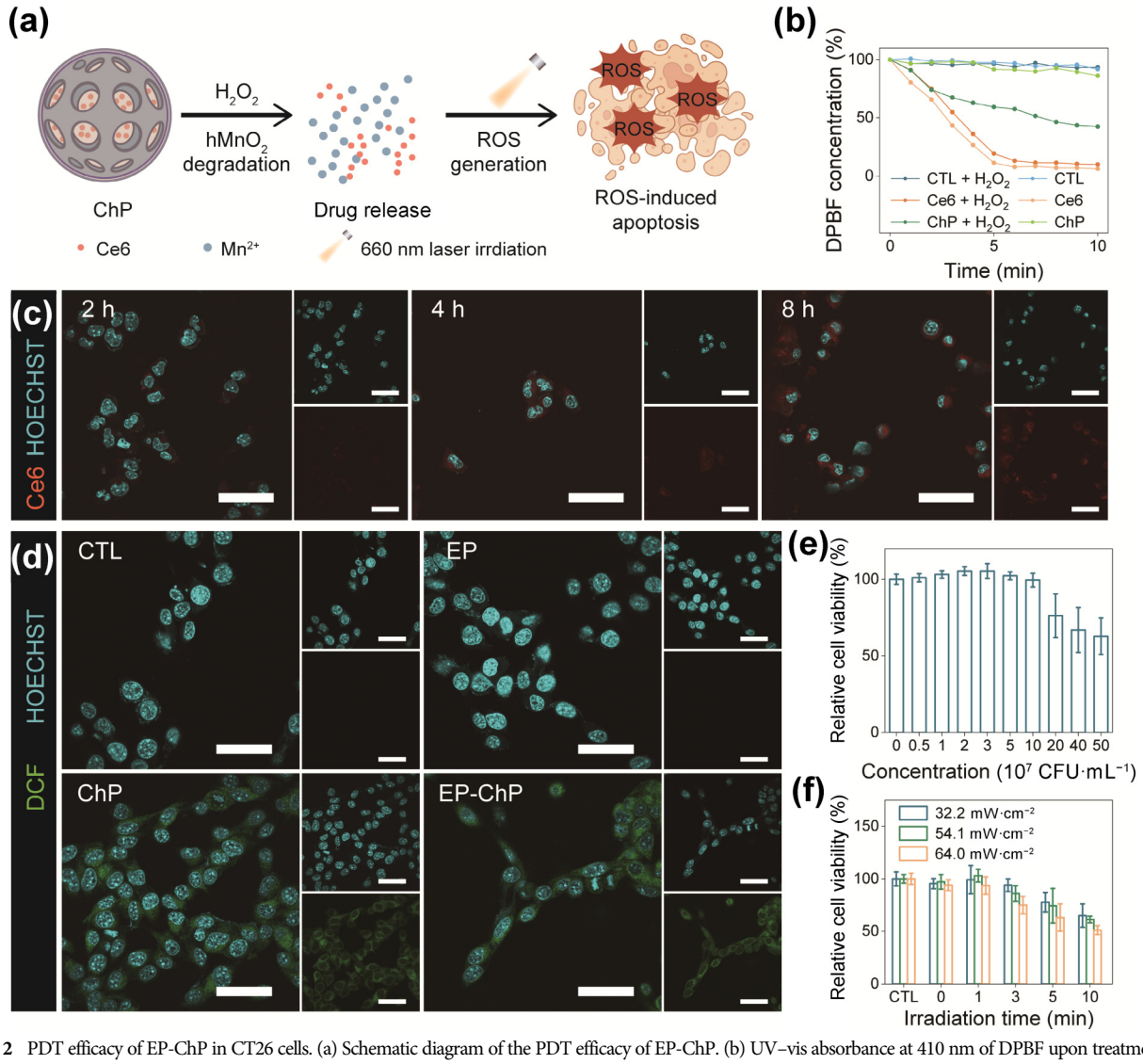

Figure 2 PDT efficacy of EP-ChP in CT26 cells. (a) Schematic diagram of the PDT efficacy of EP-ChP. (b) UV–vis absorbance at 410 nm of DPBF upon treatments with H_2O, Ce6, or ChP under a 660 nm light irradiation with or without the present of H_2O_2 solutions (100 μM). (c) The representative LSCM images of CT26 cells co-incubated with EP-ChP for various time periods. The blue and red channels indicate HOECHST and Ce6, respectively. Scale bar, 5 μm. (d) The representative LSCM images detecting intracellular ROS of CT26 cells co-incubated with PBS, EP, ChP, or EP-ChP under a 660 nm light irradiation. The blue, green, and red channels indicate HOECHST, DCF, and Ce6, respectively. Scale bar, 5 μm. (e) CCK-8 assay for CT26 cells co-incubated with EP-ChP of various concentrations. (f) CCK-8 assay for CT26 cells co-incubated with EP-ChP under a 660 nm light irradiation at various power densities for various time periods.

3.4 Enhanced PTT efficacy *in vitro*

Absorbing broadly over the range of 300–1000 nm, the pDA-coated bacteria was reported for its excellent photothermal properties [37, 38]. To ascertain this PDT/PTT combined nanoplatform, temperature changes (ΔT) under 808 nm light irradiation for EP suspensions with or without ChP decoration were recorded within 10 min, and ΔT of both suspensions reached ~ 15 °C with only negligible differences, confirming that the fabrication of ChP had little effect on its photothermal property (Fig. 3(a)). Furthermore, by recording ΔT of EP-ChP suspensions at various concentrations, it was found that its photothermal performance showed a concentration-dependent manner (Fig. 3(b)). The photothermal stability was also confirmed where ΔT of EP-ChP could still reach its maximum level of ~ 14 °C even after 5 cycles (Figs. 3(c) and 3(d)). As illustrated in Fig. 3(e), generated ROS under 660 nm light irradiation could efficiently attack HSPs, which would compromise the heat damage during PTT and discount its effect. Thus, enhanced PTT efficacy was expected in this synergistic nanoplatform. A same concentration of EP-ChP was applied and co-incubated with CT26 cells under 808 nm light irradiation, and CCK-8 assay showed that cell viabilities decreased in working power density- and irradiation time-dependent manners (Fig. 3(f)). And as expected, synergistic therapy of PDT/PTT showed a better therapeutic effect than PDT or PTT therapy alone. The cell viability dropped dramatically to ~ 11% after dual irradiation of both lasers, which was in sharp contrast to that of ~ 60% and ~ 40% after single irradiation of a 660 and an 808 nm laser respectively for even the same amount of irradiation time (Fig. 3(g)). The down-regulation of HSP90α was also confirmed via western blot assay, and an apparent decrease of HSP90α at protein levels could be observed after corresponding treatments, confirming improved PTT efficacy via PDT mechanisms (Figs. 3(h) and 3(i) and Fig. S7 in the ESM). Similar results were also observed in live-

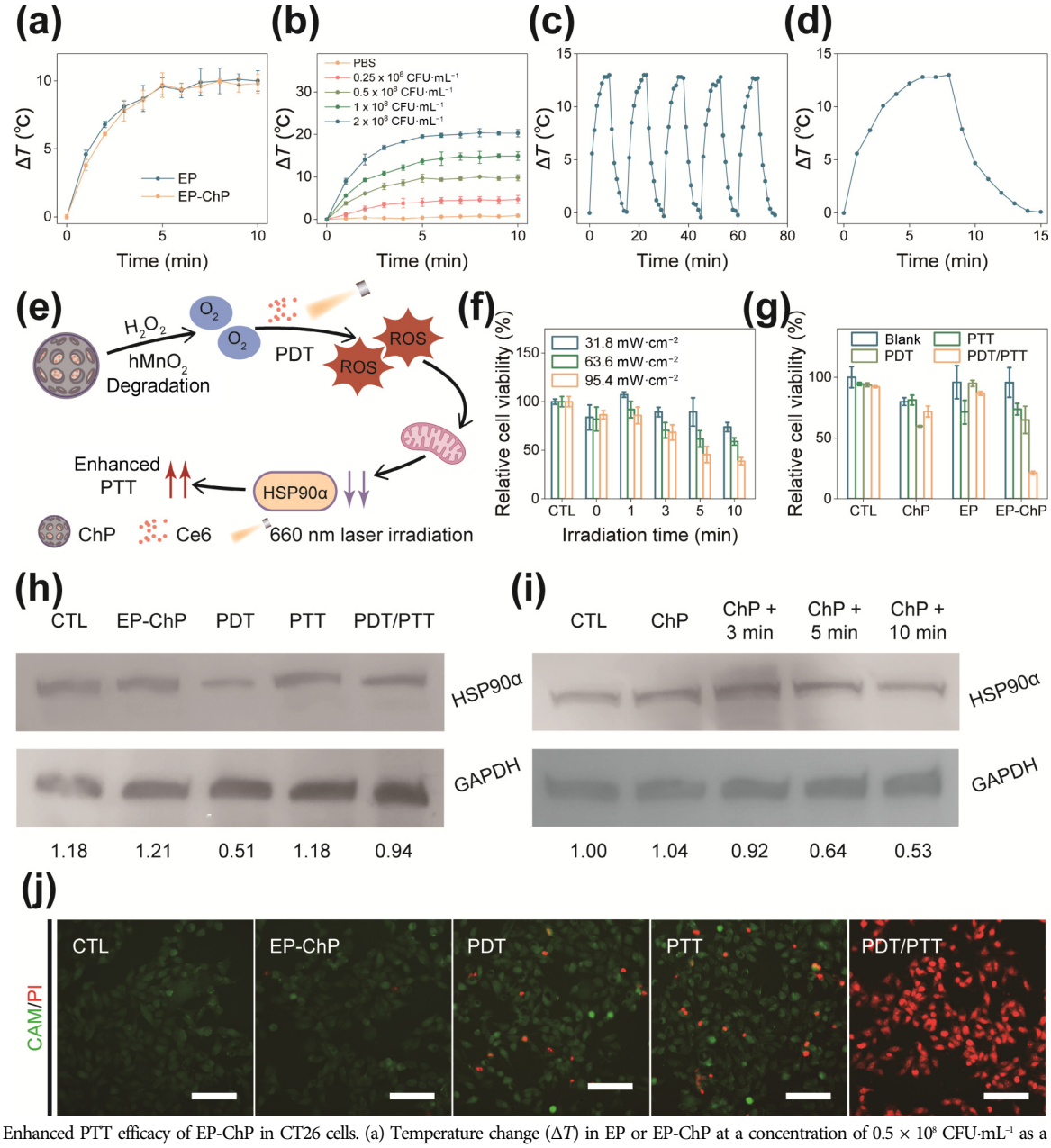

Figure 3 Enhanced PTT efficacy of EP-ChP in CT26 cells. (a) Temperature change (ΔT) in EP or EP-ChP at a concentration of 0.5 × 10^8 CFU·mL^{-1} as a function of irradiation time with an 808 nm laser at a power density was 31.8 mW·cm^{-2}. (b) ΔT in PBS or different concentrations of EP-ChP as a function of irradiation time with an 808 nm laser at a power density was 31.8 mW·cm^{-2}. (c) Photothermal conversion curves of EP-ChP at a concentration of 0.5 × 10^8 CFU·mL^{-1} under 5 cycles of irradiation with an 808 nm laser at a power density was 31.8 mW·cm^{-2}. (d) Photothermal conversion curves of EP-ChP at a concentration of 0.5 × 10^8 CFU·mL^{-1} irradiated by an 808 nm laser at a power density was 31.8 mW·cm^{-2} for 8 min. (e) Schematic diagram of enhanced PTT efficacy of EP-ChP. (f) CCK-8 assay for CT26 cells co-incubated with EP-ChP of various concentrations under an 808 nm light irradiation at various power densities for various time periods. (g) CCK-8 assay for CT26 cells co-incubated with PBS, EP, ChP, or EP-ChP under the absence, single, or dual light irradiations. (h) Western blot analysis of the HSP90α protein expression in CT26 cells co-incubated with EP-ChP under different laser irradiation. (i) Western blot analysis of the HSP90α protein expression in CT26 cells co-incubated with ChP under 660 nm laser irradiation for various time periods. (j) The representative fluorescence images of tumor cells under treatment of EP-ChP with different light irradiations. Green, Calcein AM. Red, PI. Scale bar, 200 μm.

dead cell staining assay, where dual irradiation caused more cytotoxicity to CT26 cells compared to mono irradiation along (Fig. 3(j)). These conclusions above proved the enhanced PTT efficacy as well as the synergistic efficacy against cancer cells.

3.5 *In vivo* biodistribution and temperature change in tumor tissues

Encouraged by the favorable results *in vitro*, the *in vivo* anti-tumor effect of the synergistic therapy was subsequently evaluated using BALB/c mice bearing CT26 allografts. Since EcN had been proved with preferential accumulation in the hypoxia core of tumors by aerotaxis and chemotaxis, the biodistribution of bacteria after intravenous injection through the tail vein was examined first via serial dilution plating on solid Luria–Bertani (LB) plates (Figs. 4(h)–4(j)). Little bacteria colonies could be observed in major organs (including heart, liver, spleen, lung, and kidney), which might be the result of immune elimination in non-

immunosuppressive areas, while a significantly higher amount of colonies could be observed in tumor tissues. Besides, the immunofluorescence staining of anti-*E. coli* in major organs showed the same results. Moreover, the viability of EcN colonized in tumor dropped dramatically under dual laser irradiations, eliminating the suspicion of possible sepsis. Next, the ability of EP-ChP to heat tumor tissue under an 808 nm laser irradiation was recorded. As shown in Fig. S8 in the ESM, temperature in tumor tissues rose in time- and dose-dependent manners and could easily reach up to 42.0 °C within 5 min.

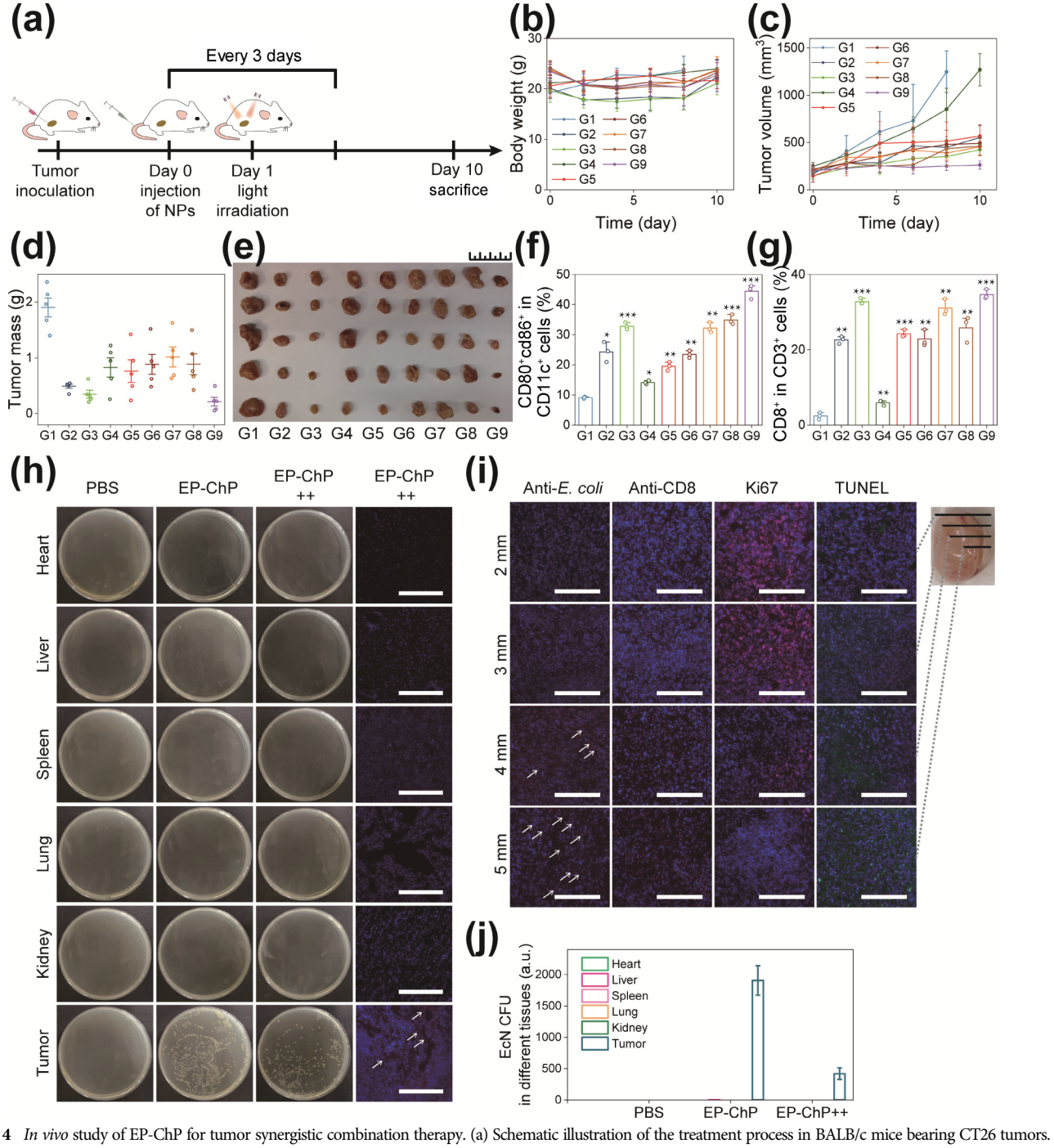

Figure 4 *In vivo* study of EP-ChP for tumor synergistic combination therapy. (a) Schematic illustration of the treatment process in BALB/c mice bearing CT26 tumors. (b) The administration of mouse body weights changes in different treatment groups. (c) and (d) The tumor volumes change and weights under different treatments. (e) The physical images of tumors under different treatments on day 10. (f) Quantification analysis of $CD80^+CD86^+$ DCs (gated on $CD11c^+$ cells) in spleen tissues after different treatments. (g) Quantification analysis of $CD8^+$ T cells (gated on $CD3^+$ T cells) in spleen tissues after different treatments. (h) Homogenates of heart, liver, spleen, lung, kidney and tumor tissues from mice with the treatment of EP-ChP with or without dual light irradiations were cultured on solid LB agar at 37 °C. And sections from corresponding organs were stained with anti-*E. coli* LPS antibody and Cy3-labeled secondary antibodies. Scale bar, 100 μm. (i) Anti-*E. coli* LPS, anti-CD8, Ki67 and TUNEL staining in transverse tumor sections at 2, 3, 4, and 5 mm. Scale bar, 100 μm. (j) Bacteria growth of EP-ChP in tumor tissues and major organs. (G1) PBS; (G2) EP; (G3) EP + 808 nm irradiation; (G4) ChP; (G5) ChP + 660 nm irradiation; (G6) EP-ChP; (G7) EP-ChP + 808 nm irradiation; (G8) EP-ChP + 660 nm irradiation; (G9) EP-ChP + dual irradiations. *$p < 0.05$, **$p < 0.01$, ***$p < 0.001$ and ****$p < 0.0001$.

3.6 Penetration of immune adjuvant and the activation of immune responses in deep tumors

To prove the hypoxia-targeted delivery of PDT/PTT system to the necrosis cores within solid tumors based on the active tumor penetrating ability of EcN, the immunofluorescence staining of *E. coli* was shown in 4 transverse sections passing through the center of the tumor, which were 2, 3, 4, and 5 mm in length respectively. More bacteria were detected in slices of 4 and 5 mm, confirming EcN homing to the center of solid tumors. Moreover, T cell infiltration within solid tumors was also evaluated via the immunofluorescence staining of anti-CD8 in corresponding transverse sections, and enhanced infiltrations within deep tumors were observed through the upregulation of effector T cells, indicating an enhanced penetration of immune adjuvant and activation of immune responses in the center of solid tumors (Fig. 4(i)). Next, the immunomodulation ability of the synergistic therapy on dendritic cells (DCs) and $CD8^+$ T cells was tested, which play an important role in immunity initiation and protective immunity respectively. Briefly, immature DCs are first recruited and stimulated to mature DCs, followed by naïve T cells activated to effector T cells. To further investigate the antitumor mechanism, we analyzed the major immune cells in the spleens of mice in all groups. And as shown in Fig. 4(f) and Fig. S9 in the ESM, flow cytometry analysis revealed that the percentage of matured DCs (gated on $CD11c^+$ and featured by $CD80^+CD86^+$) reached ~ 41.8% in the synergistic treated group in G9, which was 4.7 times higher than that of the control group of G1 (~ 8.75%). And the percentage of $CD8^+$ T cells (gated on $CD3^+$ and featured by $CD8^+$) grew from ~ 3.34% to ~ 36.1% in corresponding groups (Fig. 4(g) and Fig. S10 in the ESM), indicating a strong activation of anti-tumor immune responses. Notably, the differentiation of naïve T cells to $CD8^+$ T cells seemed to be in a bacteria-dependent instead of a phototherapy-dependent manner where all bacteria-treated groups showed relatively comparable rates, especially compared with G1 and G4. But the maturation of DCs showed a stronger relationship between phototherapy-dependent ICD than bacteria-based infection, where laser irradiation-treated groups showed a higher rate of maturity of DCs and dual laser irradiation-treated groups of G9 showed the highest maturity rate. Moreover, cell survival in different areas of the tumor was measured and a decreased cell proliferation was observed in deep tumor, indicating sufficient synergistic therapeutic effect due to the penetration depth of bacteria. In summary, the bacteria-based phototherapy nanoplatform demonstrated great potential for the combined therapy of PDT and PTT to activate the immune responses and eliminate tumors *in vivo*.

3.7 *In vivo* anti-tumor effect

Drawing on the experimental results mentioned above, mice bearing CT26 allografts were randomly divided into 9 groups for different treatments: (G1) PBS; (G2) EP; (G3) EP + 808 nm irradiation; (G4) ChP; (G5) ChP + 660 nm irradiation; (G6) EP-ChP; (G7) EP-ChP + 808 nm irradiation; (G8) EP-ChP + 660 nm irradiation; (G9) EP-ChP + dual irradiations. All mice were irradiated via corresponding laser following intravenous injection (Fig. 4(a)), and the tumor inhibition study was carried out by assessing body weights and tumor volumes under different treatments in 10 days (Figs. 4(b) and 4(c)). The tumor volumes of all groups treated with EP-ChP with irradiation (660 nm laser or 808 nm laser along, or dual lasers) showed a visible inhibition of tumor growth while a rapid growth trend could be found in other groups, especially in the PBS group and groups without bacteria or irradiation. Notably, xenografts are mostly eliminated in mice treated with EP-ChP upon dual laser irradiations, which indicates a better therapeutic effect for the combined therapy of PDT and PTT. On day 10, all mice were sacrificed and all tumors were collected, weighed, and photographed for further confirmation of combined antitumor efficacy (Figs. 4(d) and 4(e)). In addition, the hematoxylin and eosin (H&E) staining of major organs (hearts, livers, spleens, lungs, and kidneys) of mice in all groups were observed and no appreciable abnormality is found (Fig. S11 in the ESM). Further analyses of anti-CD8, TUNEL, Ki67 and H&E staining of tumor tissues of mice in all groups were shown in Fig. S12 in the ESM, where a decreased cell density and proliferation in G9 similarly showed the synergistic therapeutic effect and indicated stronger immune responses in tumor areas. Moreover, both the biodistribution of bacteria and routine blood biochemical indexes on day 10 were monitored (Figs. S13 and S14 in the ESM). The clearance of *in vivo* bacteria and the limited damages to the liver and kidney indicated minimal toxicity of the bacteria-based administrations.

4 Conclusions

In summary, we proposed a bacteria-based nanoplatform of EP-ChP for the co-delivery of combined phototherapy triggered by dual laser irradiations and studied its synergistic immunologic responses on primary tumors. This therapeutic strategy heavily relied on the ability of the tumor-targeting preference of EcN to hypoxia cores of tumor tissues, which worked as the carrier of both PDT and PTT agents. PDA-coating improved biocompatibility and provided it with efficient photothermal properties. Ce6 was loaded in the TME-responsive nanoparticles of $hMnO_2$ and a PEI-coating enabled its fabrication to pDA-coated bacteria. Upon dual irradiations of both 660 and 808 nm lasers, combined therapy of PDT and PTT with an ideal tumor targeting efficiency was performed and stronger activation of ICD was realized, which was featured by an increase of anti-tumor immune cells *in vivo*. Moreover, EcN also worked as an immune agent and potentially enhanced TME immunogenicity. As a result, a strengthened and synergetic antitumor immune response was elicited in the immunosuppressive tumor areas, compared to a relatively weak response in a single therapy. Collectively, this therapeutic strategy offered a promising option for immunotherapy within deep tumors for the elimination of primary tumors.

Electronic Supplementary Material: Supplementary material (further details of growth of bacteria and cells, preparation and characterization of hollow MnO_2, photothermal performance of EP and EP-ChP *in vitro*, cell viabilities of EP-ChP *in vitro*, and western blot assay) is available in the online version of this article at https://doi.org/10.26599/NR.2025.94907081.

Data availability

All data needed to support the conclusions in the paper are presented in the manuscript and the Electronic Supplementary

Material. Additional data related to this paper may be requested from the corresponding author upon request.

Acknowledgements

This work was supported by the National Key R&D Program of China (No. 2019YFA0709200), the National Natural Science Foundation of China (Nos. 22477056 and 82472379), the Fundamental Research Funds for Central Universities, the Natural Science Foundation of Jiangsu Province (No. BK20200336), the Key Research and Development Program of Jiangsu Province (No. BE2021373), the Program for Innovative Talents and Entrepreneur in Jiangsu, and the Postgraduate Research & Practice Innovation Program of Jiangsu Province (No. KYCV20_0036).

Declaration of competing interest

The authors declare no conflict of interest.

Author contribution statement

Y. J. S.: Conceptualization, project administration, supervision, resources, funding acquisition, and writing – review & editing. J. J. Y.: Supervision, resources, and funding acquisition. J. T.: Supervision, resources, and funding acquisition. B. S. H.: Supervision, resources, and funding acquisition. W. L.: Investigation, validation, visualization, and writing – original draft. S. Y. D.: Validation and visualization. Y. T. J.: Validation and visualization. All the authors have approved the final manuscript.

Informed consent

Not applicable.

Ethics statement

All animal procedures were approved and compiled with the guidelines of the Institutional Animal Care and Ethics Committee of Nanjing University (ethical approval number: IACUC-2303005).

Use of AI statement

None.

References

[1] Waldman, A. D.; Fritz, J. M.; Lenardo, M. J. A guide to cancer immunotherapy: From T cell basic science to clinical practice. *Nat. Rev. Immunol.* **2020**, *20*, 651–668.

[2] Singh, A. K.; McGuirk, J. P. CAR T cells: Continuation in a revolution of immunotherapy. *Lancet Oncol.* **2020**, *21*, e168–e178.

[3] Vitale, I.; Shema, E.; Loi, S.; Galluzzi, L. Intratumoral heterogeneity in cancer progression and response to immunotherapy. *Nat. Med.* **2021**, *27*, 212–224.

[4] Bonaventura, P.; Shekarian, T.; Alcazer, V.; Valladeau-Guilemond, J.; Valsesia-Wittmann, S.; Amigorena, S.; Caux, C.; Depil, S. Cold tumors: A therapeutic challenge for immunotherapy. *Front. Immunol.* **2019**, *10*, 168.

[5] Binnewies, M.; Roberts, E. W.; Kersten, K.; Chan, V.; Fearon, D. F.; Merad, M.; Coussens, L. M.; Gabrilovich, D. I.; Ostrand-Rosenberg, S.; Hedrick, C. C. et al. Understanding the tumor immune microenvironment (TIME) for effective therapy. *Nat. Med.* **2018**, *24*, 541–550.

[6] Yang, Z.; Gao, D.; Zhao, J.; Yang, G. J.; Guo, M.; Wang, Y.; Ren, X. C.; Kim, J. S.; Jin, L.; Tian, Z. M. et al. Thermal immunonanomedicine in cancer. *Nat. Rev. Clin. Oncol.* **2023**, *20*, 116–134.

[7] Wang, J. R.; Zhang, W. L.; Xie, Z. Y.; Wang, X. Y.; Luo, Y.; Jiang, W. X.; Liu, Y.; Wang, Z. G.; Ran, H. T.; Song, W. X. et al. Magnetic nanodroplets for enhanced deep penetration of solid tumors and simultaneous magnetothermal-sensitized immunotherapy against tumor proliferation and metastasis. *Adv. Healthc. Mater.* **2022**, *11*, 2201399.

[8] Drake, C. G.; Lipson, E. J.; Brahmer, J. R. Regulatory T cells-an important target for cancer immunotherapy. *Nat. Rev. Clin. Oncol.* **2014**, *11*, 307.

[9] Dane, E. L.; Belessiotis-Richards, A.; Backlund, C.; Wang, J. N.; Hidaka, K.; Milling, L. E.; Bhagchandani, S.; Melo, M. B.; Wu, S. W.; Li, N. et al. STING agonist delivery by tumour-penetrating PEG-lipid nanodiscs primes robust anticancer immunity. *Nat. Mater.* **2022**, *21*, 710–720.

[10] Hao, M. X.; Zhu, L. L.; Hou, S. Y.; Chen, S. J.; Li, X. Q.; Li, K. M.; Zhu, N. C.; Chen, S. S.; Xue, L. J.; Ju, C. Y. et al. Sensitizing tumors to immune checkpoint blockage via STING agonists delivered by tumor-penetrating neutrophil cytopharmaceuticals. *ACS Nano* **2023**, *17*, 1663–1680.

[11] Chen, H.; Shi, T.; Wang, Y.; Liu, Z. Y.; Liu, F. C.; Zhang, H. Y.; Wang, X. W.; Miao, Z. Y.; Liu, B. R.; Wan, M. M. et al. Deep penetration of nanolevel drugs and micrometer-level T Cells promoted by nanomotors for cancer immunochemotherapy. *J. Am. Chem. Soc.* **2021**, *143*, 12025–12037.

[12] Zhao, Y.; Fu, X.; Lopez, J. I.; Rowan, A.; Au, L.; Fendler, A.; Hazell, S.; Xu, H.; Horswell, S.; Shepherd, S. T. C. et al. Selection of metastasis competent subclones in the tumour interior. *Nat. Ecol. Evol.* **2021**, *5*, 1033–1045.

[13] Brown, J. M.; Wilson, W. R. Exploiting tumour hypoxia in cancer treatment. *Nat. Rev. Cancer* **2004**, *4*, 437–447.

[14] Sepich-Poore, G. D.; Zitvogel, L.; Straussman, R.; Hasty, J.; Wargo, J. A.; Knight, R. The microbiome and human cancer. *Science* **2021**, *371*, eabc4552.

[15] Luo, C. H.; Huang, C. T.; Su, C. H.; Yeh, C. S. Bacteria-mediated hypoxia-specific delivery of nanoparticles for tumors imaging and therapy. *Nano Lett.* **2016**, *16*, 3493–3499.

[16] Chen, Q. W.; Liu, X. H.; Fan, J. X.; Peng, S. Y.; Wang, J. W.; Wang, X. N.; Zhang, C.; Liu, C. J.; Zhang, X. Z. Self-mineralized photothermal bacteria hybridizing with mitochondria-targeted metal-organic frameworks for augmenting photothermal tumor therapy. *Adv. Funct. Mater.* **2020**, *30*, 1909806.

[17] Singh, A. V.; Hosseinidoust, Z.; Park, B. W.; Yasa, O.; Sitti, M. Microemulsion-based soft bacteria-driven microswimmers for active cargo delivery. *ACS Nano* **2017**, *11*, 9759–9769.

[18] Chu, B. B.; Yang, Y. M.; Tang, J. L.; Song, B.; He, Y.; Wang, H. Y. Trojan nanobacteria system for photothermal programmable destruction of deep tumor tissues. *Angew. Chem., Int. Ed.* **2022**, *61*, e202208422.

[19] Zheng, D. W.; Chen, Y.; Li, Z. H.; Xu, L.; Li, C. X.; Li, B.; Fan, J. X.; Cheng, S. X.; Zhang, X. Z. Optically-controlled bacterial metabolite for cancer therapy. *Nat. Commun.* **2018**, *9*, 1680.

[20] Felfoul, O.; Mohammadi, M.; Taherkhani, S.; De Lanauze, D.; Xu, Y. Z.; Loghin, D.; Essa, S.; Jancik, S.; Houle, D.; Lafleur, M. et al. Magneto-aerotactic bacteria deliver drug-containing nanoliposomes to tumour hypoxic regions. *Nat. Nanotechnol.* **2016**, *11*, 941–947.

[21] Kim, O. Y.; Park, H. T.; Dinh, N. T. H.; Choi, S. J.; Lee, J.; Kim, J. H.; Lee, S. W.; Gho, Y. S. Bacterial outer membrane vesicles suppress tumor by interferon-γ-mediated antitumor response. *Nat. Commun.* **2017**, *8*, 626.

[22] Geng, Z. M.; Cao, Z. P.; Liu, R.; Liu, K.; Liu, J. Y.; Tan, W. H. Aptamer-assisted tumor localization of bacteria for enhanced biotherapy. *Nat. Commun.* **2021**, *12*, 6584.

[23] Arias-Alpizar, G.; Kong, L.; Vlieg, R. C.; Rabe, A.; Papadopoulou, P.;

Meijer, M. S.; Bonnet, S.; Vogel, S.; Van Noort, J.; Kros, A. et al. Light-triggered switching of liposome surface charge directs delivery of membrane impermeable payloads *in vivo*. *Nat. Commun.* **2020**, *11*, 3638.

[24] Liu, J.; Chang, J.; Jiang, Y.; Meng, X. D.; Sun, T. M.; Mao, L. Q.; Xu, Q. B.; Wang, M. Fast and efficient CRISPR/Cas9 genome editing *in vivo* enabled by bioreducible lipid and messenger RNA nanoparticles. *Adv. Mater.* **2019**, *31*, 1902575.

[25] Wu, X. L.; Yue, H.; Zhang, Y. Y.; Gao, X. Y.; Li, X. Y.; Wang, L. C.; Cao, Y. F.; Hou, M.; An, H. X.; Zhang, L. et al. Packaging and delivering enzymes by amorphous metal-organic frameworks. *Nat. Commun.* **2019**, *10*, 5165.

[26] Alyami, M. Z.; Alsaiari, S. K.; Li, Y. Y.; Qutub, S. S.; Aleisa, F. A.; Sougrat, R.; Merzaban, J. S.; Khashab, N. M. Cell-type-specific CRISPR/Cas9 delivery by biomimetic metal organic frameworks. *J. Am. Chem. Soc.* **2020**, *142*, 1715–1720.

[27] Minchinton, A. I.; Tannock, I. F. Drug penetration in solid tumours. *Nat. Rev. Cancer* **2006**, *6*, 583–592.

[28] Wilson, W. R.; Hay, M. P. Targeting hypoxia in cancer therapy. *Nat. Rev. Cancer* **2011**, *11*, 393–410.

[29] Li, X. S.; Lovell, J. F.; Yoon, J.; Chen, X. Y. Clinical development and potential of photothermal and photodynamic therapies for cancer. *Nat. Rev. Clin. Oncol.* **2020**, *17*, 657–674.

[30] Deng, S. H.; Li, X. X.; Liu, S.; Chen, J. F.; Li, M. Q.; Chew, S. Y.; Leong, K. W.; Cheng, D. Codelivery of CRISPR-Cas9 and chlorin e6 for spatially controlled tumor-specific gene editing with synergistic drug effects. *Sci. Adv.* **2020**, *6*, eabb4005.

[31] Yang, J. X.; Hou, M. F.; Sun, W. S.; Wu, Q. H.; Xu, J.; Xiong, L. Q.; Chai, Y. M.; Liu, Y. X.; Yu, M. H.; Wang, H. L. et al. Sequential PDT and PTT using dual-modal single-walled carbon nanohorns synergistically promote systemic immune responses against tumor metastasis and relapse. *Adv. Sci.* **2020**, *7*, 2001088.

[32] Li, W.; Yang, J.; Luo, L. H.; Jiang, M. S.; Qin, B.; Yin, H.; Zhu, C. Q.; Yuan, X. L.; Zhang, J. L.; Luo, Z. Y. et al. Targeting photodynamic and photothermal therapy to the endoplasmic reticulum enhances immunogenic cancer cell death. *Nat. Commun.* **2019**, *10*, 3349.

[33] Cheng, Q.; Li, Z. H.; Sun, Y. X.; Zhang, X. Z. Controlled synthesis of a core–shell nanohybrid for effective multimodal image-guided combined photothermal/photodynamic therapy of tumors. *NPG Asia Mater.* **2019**, *11*, 63.

[34] Wen, Z. F.; Liu, F. Y.; Liu, G. X.; Sun, Q. Y.; Zhang, Y. H.; Muhammad, M.; Xu, Y. Q.; Li, H. J.; Sun, S. G. Assembly of multifunction dyes and heat shock protein 90 inhibitor coupled to bovine serum albumin in nanoparticles for multimodal photodynamic/photothermal/chemo-therapy. *J. Colloid Interface Sci.* **2021**, *590*, 290–300.

[35] Wei, J. P.; Li, J. C.; Sun, D.; Li, Q.; Ma, J. Y.; Chen, X. L.; Zhu, X.; Zheng, N. F. A novel theranostic nanoplatform based on Pd@Pt-PEG-Ce6 for enhanced photodynamic therapy by modulating tumor hypoxia microenvironment. *Adv. Funct. Mater.* **2018**, *28*, 1706310.

[36] Yang, G. B.; Xu, L. G.; Chao, Y.; Xu, J.; Sun, X. Q.; Wu, Y. F.; Peng, R.; Liu, Z. Hollow MnO_2 as a tumor-microenvironment-responsive biodegradable nano-platform for combination therapy favoring antitumor immune responses. *Nat. Commun.* **2017**, *8*, 902.

[37] Chen, W. F.; Wang, Y.; Qin, M.; Zhang, X. D.; Zhang, Z. R.; Sun, X.; Gu, Z. Bacteria-driven hypoxia targeting for combined biotherapy and photothermal therapy. *ACS Nano* **2018**, *12*, 5995–6005.

[38] Li, J. J.; Xia, Q.; Guo, H. Y.; Fu, Z. Z.; Liu, Y.; Lin, S. S.; Liu, J. Y. Decorating bacteria with triple immune nanoactivators generates tumor-resident living immunotherapeutics. *Angew. Chem., Int. Ed.* **2022**, *61*, e202202409.

[39] Huang, C. L.; Zhang, L.; Guo, Q.; Zuo, Y. Y.; Wang, N. N.; Wang, H.; Kong, D. L.; Zhu, D. W.; Zhang, L. H. Robust nanovaccine based on polydopamine-coated mesoporous silica nanoparticles for effective photothermal-immunotherapy against melanoma. *Adv. Funct. Mater.* **2021**, *31*, 2010637.

[40] Wei, R. X.; Gong, X. Q.; Lin, H. Y.; Zhang, K.; Li, A.; Liu, K.; Shan, H.; Chen, X. Y.; Gao, J. H. Versatile octapod-shaped hollow porous manganese(II) oxide nanoplatform for real-time visualization of cargo delivery. *Nano Lett.* **2019**, *19*, 5394–5402.

[41] Chouaib, S.; Noman, M. Z.; Kosmatopoulos, K.; Curran, M. A. Hypoxic stress: Obstacles and opportunities for innovative immunotherapy of cancer. *Oncogene* **2017**, *36*, 439–445.

[42] Chang, C. H.; Qiu, J.; O'Sullivan, D.; Buck, M. D.; Noguchi, T.; Curtis, J. D.; Chen, Q. Y.; Gindin, M.; Gubin, M. M.; Van Der Windt, G. J. W. et al. Metabolic competition in the tumor microenvironment is a driver of cancer progression. *Cell* **2015**, *162*, 1229–1241.